NANO LETTERS

Letter

pubs.acs.org/NanoLett

Chloride Incorporation Process in $CH_3NH_3PbI_{3-x}Cl_x$ Perovskites via Nanoscale Bandgap Maps

Jungseok Chae,[†,‡] Qingfeng Dong,[§] Jinsong Huang,*[,§] and Andrea Centrone*[,†]

[†]Center for Nanoscale Science and Technology, National Institute of Standards and Technology, 100 Bureau Drive, Gaithersburg, Maryland 20899, United States

[‡]Maryland Nanocenter, University of Maryland, College Park, Maryland 20742 United States

[§]Department of Mechanical and Materials Engineering, University of Nebraska-Lincoln, Lincoln, Nebraska 68588-0656, United States

Supporting Information

ABSTRACT: $CH_3NH_3PbI_{3-x}Cl_x$ perovskites enable fabrication of highly efficient solar cells. Chloride ions benefit the morphology, carrier diffusion length, and stability of perovskite films; however, whether those benefits stem from the presence of Cl^- in the precursor solution or from their incorporation in annealed films is debated. In this work, the photothermal-induced resonance, an in situ technique with nanoscale resolution, is leveraged to measure the bandgap of $CH_3NH_3PbI_{3-x}Cl_x$ films obtained by a multicycle coating process that produces high efficiency (~16%) solar cells. Because chloride ions modify the perovskite lattice, thereby widening the bandgap, measuring the bandgap locally yields the local chloride content. After a mild annealing (60 min, 60 °C) the films consist of Cl-rich ($x < 0.3$) and Cl-poor phases that upon further annealing (110 °C) evolve into a homogeneous Cl-poorer ($x < 0.06$) phase, suggesting that methylammonium-chrloride is progressively expelled from the film. Despite the small chloride content, $CH_3NH_3PbI_{3-x}Cl_x$ films show better thermal stability up to 140 °C with respect $CH_3NH_3PbI_3$ films fabricated with the same methodology.

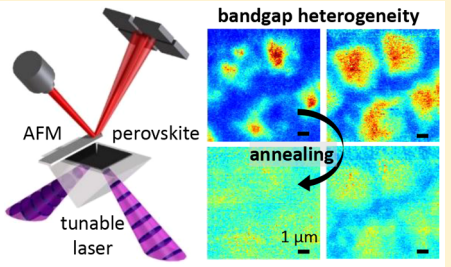

KEYWORDS: *Mixed-halide organolead perovskites, PTIR, bandgap, nanoscale mapping, solar cells*

The pace of improvement in the energy conversion efficiency of organometal trihalide perovskite solar cells has been unprecedented.[1−5] The remarkable photovoltaic performance of these materials is related to the exceptionally long carrier diffusion lengths in both thin films and single crystals.[6−9] Pioneering work from Snaith and co-workers introduced planar heterojunction perovskite solar cells made by a compound with the general formula $CH_3NH_3PbI_{3-x}Cl_x$, obtained by the reaction of lead chloride ($PbCl_2$) with methylammonium iodide (CH_3NH_3I, hereafter MAI).[10] Since then, $MAPbI_{3-x}Cl_x$ compounds (where MA = $CH_3NH_3^+$) have been widely studied, leading to solar cell devices with steady-state efficiencies up to 19%.[11,12] However, the role of chloride ions (Cl^-) in the fabrication and performance of both thermally evaporated and solution-processed $MAPbI_{3-x}Cl_x$ solar cells is still unclear and heavily debated to the point that even the incorporation of Cl^- has been questioned.[13] For example, trace amounts of Cl (~1% mol/mol Cl/I molar ratio) were detected in annealed films, either within 20 nm of the film top surface by X-ray photoelectron spectroscopy (XPS)[14] or in close proximity to the perovskite/TiO_2 interface by X-ray fluorescence[15] and angle-resolved XPS.[16] In another study using scanning transmission electron microscopy with energy dispersive spectroscopy (STEM-EDS), it was suggested that the Cl/I molar ratio is below the STEM-EDS detection limit (~0.1%), implying that practically no Cl^- is incorporated in the annealed material.[13] These results contrast with XPS data obtained on perovskite films fabricated by multilayer deposition that indicate a much larger Cl content (up to ~8.3% mol/mol Cl/I).[17,18]

What is generally accepted is that despite the high Cl content in the precursor solutions (e.g., $MAI/PbCl_2 = 3:1$)[14,19] the bandgap (~1.60 eV) and the Cl/I molar ratio in $MAPbI_{3-x}Cl_x$ annealed films cannot be tuned widely. For example, it was suggested theoretically that the upper limit for the Cl/I molar ratio should be ~4% mol/mol.[19] However, it is also known that Cl ions in the precursor solution have somehow a profound and beneficial effect on the film morphology,[13,14,20] carrier diffusion length,[6] and stability.[17] For example, the discovery that the diffusion lengths of holes and electrons in $MAPbI_{3-x}Cl_x$ are well balanced and exceed 1 μm[6] sparked a tremendous interest in these compounds. Because of these experiments and other observations, it is generally believed that Cl leaves the perovskite film as methylammonium chloride (MACl) in the thermal annealing process.[14,15,19,20] Several studies suggested that the chloride ions in the precursor solution slow down the nucleation and growth of perovskite crystals, resulting in more continuous and better quality films.[14,20,21] However, because of the small amount of Cl^- incorporated in annealed films, its

Received: September 3, 2015
Revised: October 22, 2015
Published: November 3, 2015

DOI: 10.1021/acs.nanolett.5b03556
Nano Lett. 2015, 15, 8114−8121

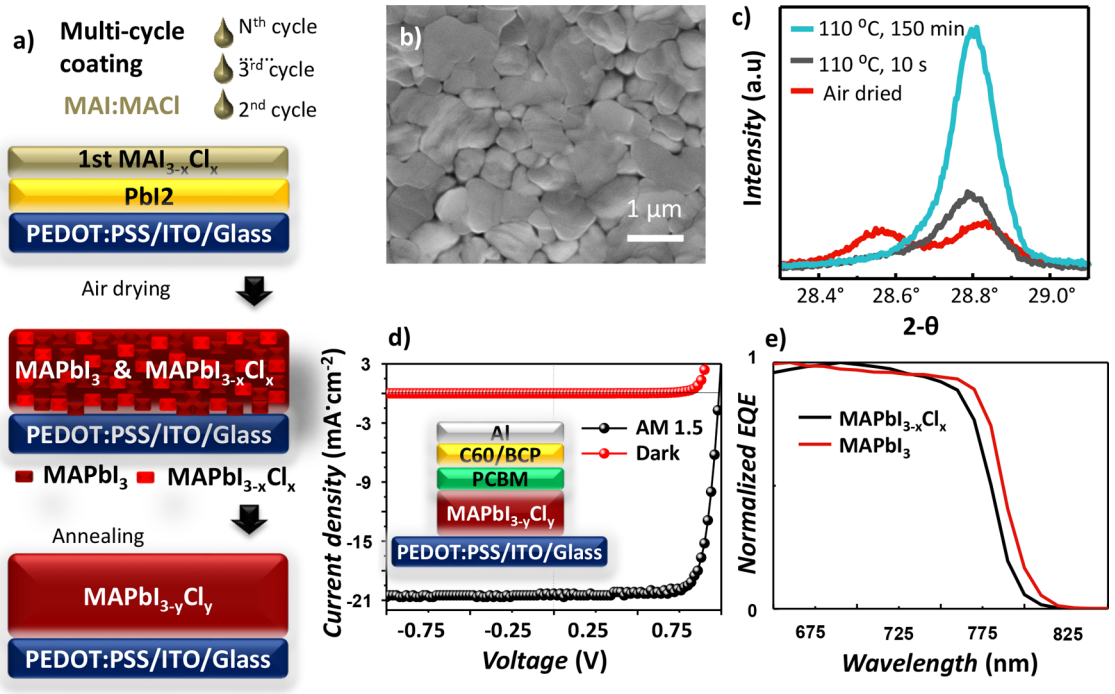

Figure 1. Formation and characterization of perovskite films. (a) Illustration of the multicycle coating method used to fabricate the $MAPbI_{3-y}Cl_y$ perovskite layer (thickness ~575 nm) that requires the sequential deposition of a PbI_2 layer and then multiple cycles of MAI/MACl layers. (b) SEM of image of a $MAPbI_{3-x}Cl_x$ film formed after six deposition cycles. (c) XRD patterns of an air-dried $MAPbI_{3-x}Cl_x$ film (red) and of the same film after annealing at 110 °C for 10 s (black) and 150 min (blue). (d) Typical photocurrent of a $MAPbI_{3-x}Cl_x$ based solar cell. The inset illustrates the solar cell structure. (e) Typical EQE spectra of $MAPbI_{3-x}Cl_x$ and $MAPbI_3$ based perovskite solar cells in which the perovskite layer was annealed at 110 °C for 90 min.

influence on perovskite solar cells performance has remained elusive. In particular, a recent in situ study suggested that the Cl^- content in perovskite films decreases during annealing and that the resulting $MAPbI_{3-x}Cl_x$ phase (Cl/I < 0.5% mol/mol) grows at the expense of a precursor phase with a higher Cl content.[15] In this case, Cl^- was detected in the film even after prolonged annealing time (95 °C, 120 min); however, no high spatial resolution images of the precursor phase and its evolution has been provided yet.

In this work, photothermal induced resonance (PTIR), a composition sensitive scanning probe technique, was used to map with nanoscale spatial resolution the bandgap in $MAPbI_{3-x}Cl_x$ films obtained with a multicycle coating process that produces high efficiency perovskite solar cells (~16%). Because chloride ions within the perovskite structure alter the lattice constants and widen the bandgap,[12] the local bandgap is directly related to the local Cl^- content in the film. Consequently, the local bandgap measured by PTIR provides a means to follow the fate of Cl^- in the perovskite films as a function of annealing. After a mild annealing (60 °C, 60 min) the film consists of a mixture of Cl-rich (x^{local} < 0.3) and Cl-poor phases that upon further annealing (110 °C) evolve into a homogeneous Cl-poorer (x^{local} < 0.06) phase, suggesting that MACl is expelled during the thermal treatment. This analysis is corroborated by macroscale X-ray diffraction (XRD) experiments. Additionally, PTIR data suggest that $MAPbI_{3-x}Cl_x$ films are significantly more stable than equivalent $MAPbI_3$ obtained with the same methodology when subjected to high temperature (140 °C) annealing.

$MAPbI_{3-x}Cl_x$ samples were prepared as illustrated in Figure 1a by a multicycle spin-coating process[12] using precursor solutions in two solvents, *N*,*N*-dimethylformamide (DMF) and 2-propanol that are orthogonal with respect to the PbI_2 solubility. In the first cycle, a PbI_2 layer was spun cast from DMF solution onto a poly(3,4-ethylenedioxythiophene)-poly-(styrenesulfonate) (PEDOT:PSS) coated substrate consisting of either indium tin oxide (ITO) on glass or ZnS optical prism (required for the PTIR experiments). Then a MAI/MACl (4:1 molar ratio) 2-propanol solution was spun cast on the PbI_2 layer in six coating-cycles by dripping 10 μL of solution every 3 s (see Experimental Section for details). The films were then transferred to a preheated hot plate for drying. The temperature and the time of this initial annealing step were varied depending on the sample and purpose. Samples annealed at 110 °C up to 150 min were used to prepare high efficiency $MAPbI_{3-x}Cl_x$ solar cell devices to test the film stability under high temperature (140 °C) annealing and to determine macroscopic film crystallinity with XRD. To better capture the evolution of Cl^- content in the $MAPbI_{3-x}Cl_x$ films with PTIR, a $MAPbI_{3-x}Cl_x$ sample on a ZnS prism was annealed under milder conditions (60 °C, 60 min) and later was subjected to subsequent annealing cycles in situ (see Table S1 of the Supporting Information). This annealing sequence allows determining the effect of annealing on the local bandgap (i.e., on the local Cl content). A $MAPbI_3$ sample was-prepared and used as a reference to measure the local bandgap and to test the high temperature (140 °C) material stability with PTIR. This $MAPbI_3$ sample was obtained on a ZnS prism from PbI_2 and MAI (in place of MAI:MACl) precursor solutions and annealed at 105 °C for 60 min.

The $MAPbI_{3-x}Cl_x$ film (Figure 1b) exhibits large grains that are typical of perovskites obtained with the multicycle coating process. Such large grains reduce charge recombination at the grain boundaries and favor the incorporation of Cl^- in the

DOI: 10.1021/acs.nanolett.5b03556
Nano Lett. 2015, 15, 8114−8121

perovskite films.[12] To begin, we measured the incorporation of Cl^- in the perovskite structure by monitoring structural changes in the film with XRD (Figure 1c). The film fully dried at room temperature shows two diffraction peaks at 28.56° and at 28.83° that can be assigned to the (220) reflection of $MAPbI_3$ and $MAPbI_{3-x}Cl_x$, respectively, suggesting that the film consists of a mixture of the two phases. The full XRD patterns (Supporting Information Figure S1) show splitting for other main peaks such as (110), (310), and (224) and show that no other phases are present. After annealing, the (220) peak of $MAPbI_3$ disappears, and the (220) peak of $MAPbI_{3-x}Cl_x$ increases in intensity and shifts to 28.79°, suggesting that annealing promotes the diffusion of Cl^- from the $MAPbI_{3-x}Cl_x$ to the $MAPbI_3$ yielding a mixed-halide $MAPbI_{3-y}Cl_y$ ($y < x$) phase. The observation of crystalline $MAPbI_3$ in the films after spin-coating could be favored by the stoichiometric excess of I^- in the precursor solutions or by faster crystallization kinetics with respect to the mixed halide phase. Consequently, thermal annealing is necessary to obtain an entirely mixed halide film.

Thanks to the continuous $MAPbI_{3-x}Cl_x$ layer high efficiency planar heterojunction solar cells can be obtained. Figure 1d shows the typical photocurrent for a perovskite solar cell with the following structure: ITO/PEDOT:PSS/$MAPbI_{3-x}Cl_x$ (≈ 575 nm)/PCBM (20 nm)/C_{60} (20 nm)/BCP (8 nm)/aluminum (100 nm), where PCBM = [6,6]-phenyl-C61-butyric acid methyl ester and BCP = 2,9-dimethyl-4,7-diphenyl-1,10-phenanthroline. The efficiency of such devices is ~15.3% ± 0.7%, confirming the quality of the films obtained with this fabrication method. The uncertainties on the photovoltaic efficiency represent a single standard deviation in the measurements on nominally identical devices. We previously showed that by replacing PEDOT:PSS with poly[bis(4-phenyl)(2,4,6-trimethylphenyl)amine], a hydrophobic hole transport layer, the efficiency can be increased up to 18.9%.[12] However, in this work, PEDOT:PSS was used because PEDOT:PSS covered ZnS prisms were used for the PTIR experiments. The solar cell external quantum efficiency (EQE) spectrum (Figure 1e) shows a blueshift compared to that of normally equivalent $MAPbI_3$ device, suggesting that a small amount of Cl^- must have been retained in the perovskite lattice even after annealing the device at 110 °C for more than 2 h. It is tentatively suggested that the retention of a small amount of Cl^- in the annealed film is favored by the large grains formed by the multicycle coating process. In addition to altering the perovskite lattice constants as a function of concentration, the chloride ions widens the perovskite bandgap.[12] Similarly, compositional changes of the perovskite films were relied upon for bandgap engineering of light-emitting diodes and laser applications.[22,23] Consequently, mapping of the local bandgap can in principle provide information on local Cl^- content.

To study the incorporation of chloride ions in the perovskite lattice in detail, we used the photothermal induced resonance (PTIR) technique,[24−28] a novel method that enables measuring absorption spectra and maps with nanoscale resolution. PTIR was initially developed in the mid-IR[24] and rapidly attracted interest for enabling label-free composition mapping[29−31] and material identification[32] at the nanoscale. For example, PTIR has enabled the characterization of diverse materials including biological samples,[31,33,34] plasmonic resonators,[35−37] metal−organic frameworks,[30] polymers,[27,38,39] and organic trihalide perovskites.[40,41] Very recently, we extended the PTIR technique to the visible and near-IR spectral ranges.[42] This novel setup enables the acquisition of maps and spectra of correlated topographic, vibrational (chemical), and electronic properties with a wavelength-independent resolution as high as ~20 nm.[42] Here we present the first application that benefits from the extended spectral range of our PTIR setup on a material of technological interest.

PTIR relies on a pulsed wavelength-tunable laser for illumination (spot size ~30 μm) and on a sharp AFM tip in contact with the sample as a local detector to measure light absorption with a spatial resolution much smaller than the optical diffraction limit. In our setup, the sample is illuminated at 45° via total internal reflection (Figure 2a) to minimize the

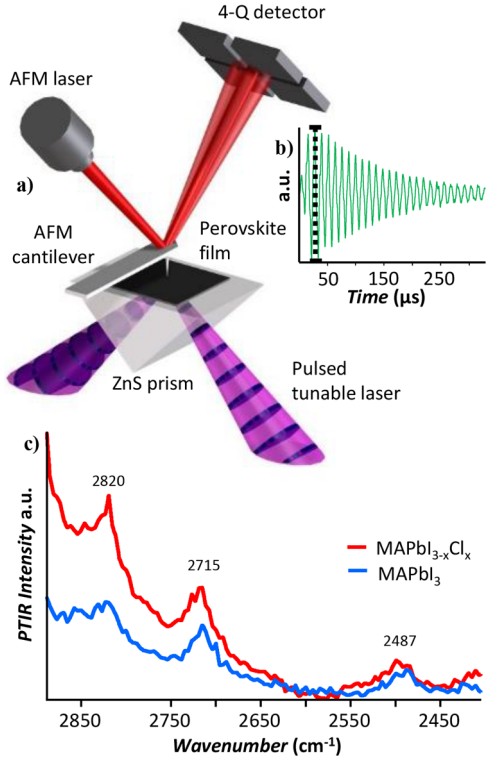

Figure 2. PTIR experimental setup. (a) Schematic of the PTIR measurement: if the sample absorbs the laser pulses (discs in purple cones) it rapidly expands deflecting the AFM cantilever whose position is monitored by the four-quadrant detector. (b) The maximum peak to peak deflection (black dotted line) is proportional to the energy absorbed by the sample and provides the PTIR signal intensity. (c) Representative vibrational PTIR spectra for $MAPbI_3$ (blue) and $MAPbI_{3-x}Cl_x$ (red) films.

light-tip direct interaction. This illumination geometry requires preparing the sample on top of an optically transparent prism. If the sample absorbs a laser pulse, it heats up and rapidly expands (faster than the AFM feedback). The function of the AFM tip is to transduce locally the sample thermal expansion, due to light absorption, into cantilever oscillations that are detected in the far-field by reflecting a diode laser into the AFM four-quadrant detector (Figure 2a). The amplitude of the cantilever oscillation (Figure 2b) is proportional to the absorbed energy but independent of scattering.[25,43] PTIR absorption spectra are obtained by maintaining the tip location fixed and by plotting the amplitude of the tip deflection as a function of wavelength. PTIR absorption maps are obtained by illuminating the sample with constant wavelength and by plotting the amplitude of the tip deflection as a function of

DOI: 10.1021/acs.nanolett.5b03556
Nano Lett. 2015, 15, 8114−8121

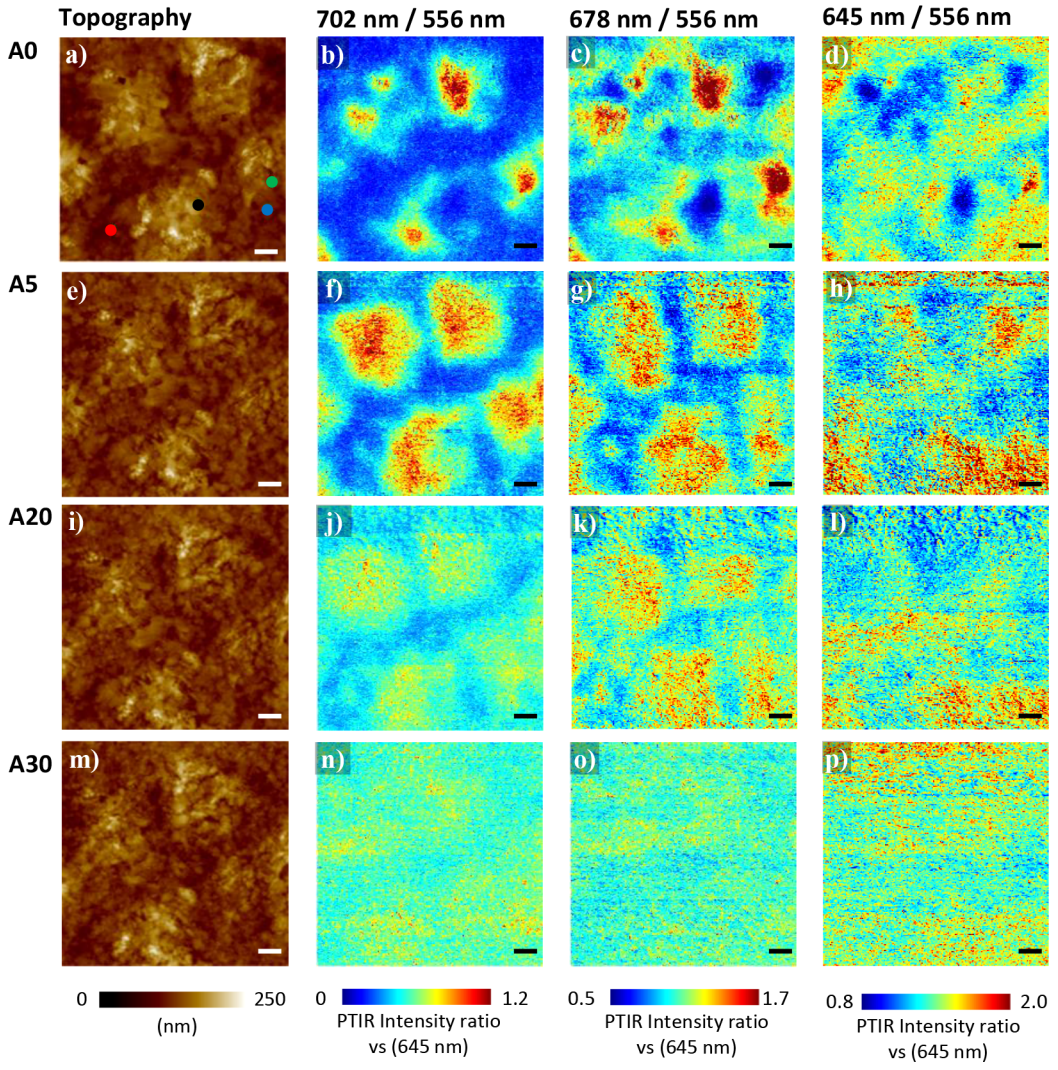

Figure 3. PTIR image ratios close to the absorption band gap in $MAPbI_{3-x}Cl_x$ mirroring the Cl^- distribution: AFM height images (first column, a, e, i, m) and PTIR absorption ratio maps (with respect to 556 nm, 2.23 eV absorption) recorded by illuminating the sample at 702 nm (1.77 eV, second column, b, f, j, n), at 678 nm (1.83 eV, third column, c, g, k, o) and at 645 nm (1.92 eV, last column, d, h, l, p). The data are displayed in rows as a function of the annealing: A0, as-prepared sample (first row, a–d), A5, after annealing at 95 °C for 5 min (second row: e–h), A20, after additional annealing at 95 °C for 5 min and at 110 °C for 10 min (third row, i–l), and A30, after additional annealing at 110 °C for 10 min (fourth row, m–p). The as-prepared sample is highly heterogeneous with Cl-poor (red tones) and Cl-rich (blue tones) regions. The sample becomes progressively more homogeneous with annealing time. The intensity of the PTIR maps are plotted with the same scale range and all scale bars are 1.0 μm. Dots in panel a mark the locations where the PTIR spectra in Figure 4 were collected.

location. A custom heating stage was used to anneal the samples in situ and all PTIR experiments were obtained by flowing nitrogen gas (0.12 dm^3/s) through a custom enclosure built around the PTIR instrument. We decided to study $MAPbI_{3-x}Cl_x$ films that had been annealed initially at low temperature (60 °C) because they retain a significant amount of Cl^-. In such films, we find that Cl is heterogeneously distributed ($\sim 0.06 < x^{local} < \sim 0.3$) initially.

The macroscale FTIR spectra of the MAI and MACl precursors (Supporting Information Figure S2a) correlate well with the nanoscale PTIR spectra of thin films obtained by solvent evaporation of the respective precursor solutions (Supporting Information Figure S2b). In particular, the combination bands at 2379 cm^{-1} (for MAI) and at 2481 cm^{-1} (for MACl) attributed to a combination of NH_3 symmetric bending and CH_3 rocking[44] and the bands at 2702 cm^{-1} (for MAI) and at 2775 cm^{-1} (for MACl), attributed to a combination of NH_3 symmetric and bending NH_3 rocking,[44] are highly sensitive to halogen counterions. In principle, in a mixed halide perovskite film those chemically specific absorption peaks could be used to map the distribution of the Cl^- and I^- ions. However, the PTIR absorption peaks of the MA^+ ions in the $MAPbI_{3-x}Cl_x$ and $MAPbI_3$ samples are weak and their spectra are hardly distinguishable (Figure 2c). This observation is not entirely surprising because the MA^+ ions in the perovskite structure have fast (few ps) rotational dynamics at room temperature,[45−50] making the bonding between MA^+ and the inorganic, negatively charged, lead-halide framework relatively weak and nondirectional.[51] Consequently, the influence of the minority Cl ions on the vibrational spectra will be on average very small unless almost complete segregation of the two halides forming the perovskite structure occurs on a length scale comparable to measurement resolution (~100 nm in this case). Because of the broad background, the PTIR chemical maps (Supporting Information Figure S3) do not show obvious heterogeneity of the perovskite film.

DOI: 10.1021/acs.nanolett.5b03556
Nano Lett. 2015, 15, 8114–8121

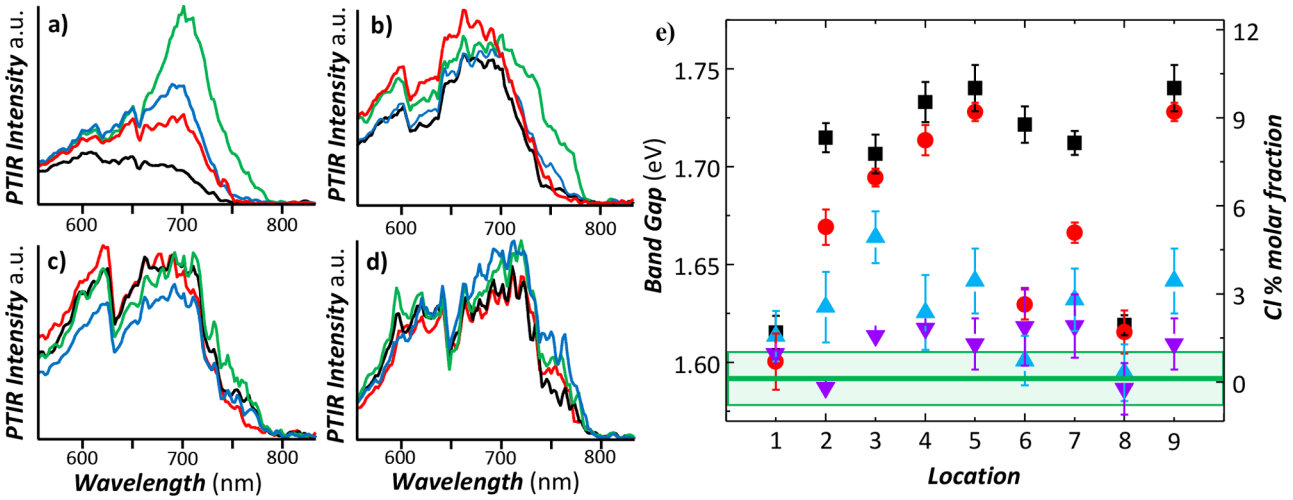

Figure 4. Local Cl content in the $MAPbI_{3-x}Cl_x$ film. (a–d) PTIR spectra obtained in selected color coded locations as indicated in Figure 3a as a function of annealing. (e) Local bandgaps (left axis) and local Cl % content (right axis) extrapolated from the linear fitting PTIR spectra from nine different locations as a function of annealing: as-prepared sample (A0, black squares), 95 °C for 5 min (A5, red circle), additional annealing at 95 °C for 5 min and at 110 °C for 10 min (A20, blue triangle), and after additional annealing at 110 °C for 10 min (A30, purple triangle). The as-prepared sample has a large variability in the local bandgap and Cl molar fraction. Upon annealing, the local bandgap and Cl content decreases at all locations, approaching the bandgap of the $MAPbI_3$ reference film (green horizontal line) for the longer annealing time. The light green rectangle and error bars represent a single standard deviation in the calculation of the local bandgap due to the linear fitting of the PTIR absorption spectra.

Although the direct detection vibrational absorption peaks that are markers for chloride ions in the perovskites films with PTIR is challenging, measurement of the bandgap is a meaningful proxy because Cl^- incorporation affects the bandgap of $MAPbI_{3-x}Cl_x$ films,[17,19] with a typical range from 1.57 to 1.63 eV.[19] For reference, the $MAPbI_3$ sample was measured first, showing PTIR visible absorption maps and spectra that are homogeneous as expected (Supporting Information Figure S4). The local absorption bandgap was obtained by linear fitting[19] of the absorption profile in the PTIR spectra. The measured local bandgap for $MAPbI_3$ was 780 nm ±7 nm (1.590 eV ± 0.013 eV), which is consistent with previous reports.[19,52] Throughout the manuscript, the uncertainty of the bandgap represents a single standard deviation in the linear fitting of the local PTIR absorption spectra.

Figure 3a–d displays the AFM topography images and the PTIR ratio maps with respect to absorption at 556 nm (2.23 eV), obtained sequentially by illuminating the $MAPbI_{3-x}Cl_x$ film at 702 nm (1.77 eV, close to the band edge), 678 nm (1.83 eV), and 645 nm (1.92 eV) over the same region for the as-prepared sample (A0). The maps at 556 nm (i.e., far from the band edge) are homogeneous (Supporting Information Figure S5) and were used as reference to obtain pixel-by-pixel ratio maps (Figure 3), which have the advantage of being independent of the sample topography (see Experimental Section for details). The measurements were repeated on the same area after sequentially annealing the sample as follows: 5 min at 95 °C (A5), additional 5 min at 95 °C and 10 min at 110 °C (A20), additional 10 min at 110 °C (A30). Spectra in selected locations also were obtained on the as-prepared sample and after each annealing step (see below). The absorption ratio maps of the as-prepared sample show progressively decreasing contrast (i.e., heterogeneity) as the photon energy increases from the band edge proximity (702 nm, Figure 3b) toward the absorption band interior (Figure 3c,d). Such heterogeneity suggests that the bandgap in the as-prepared $MAPbI_{3-x}Cl_x$ film is a function of location, most likely mirroring the heterogeneity in the local composition and crystallographic cell parameters. The ratio maps also clearly show that the spatial bandgap heterogeneity progressively decreases as a function of the annealing time. For reference the original PTIR absorption maps are reported in Supporting Information Figure S5.

The PTIR spectra obtained at selected locations (see markers in Figure 3a) before and after the sequential annealing steps are reported in Figure 4a–d. The spectra show large differences as a function of location for the as-prepared sample (Figure 4a) but become progressively more similar with annealing (Figure 4b–d). Figure 4e displays the bandgap values obtained by linearly fitting the edge of the PTIR absorption spectra in nine different locations as a function of annealing. The bandgap of as-prepared sample varies from 1.62 ± 0.01 to 1.74 ± 0.01 eV. Thus, for all the locations measured the bandgap for the $MAPbI_{3-x}Cl_x$ sample is larger than the bandgap of the $MAPbI_3$ reference sample and much smaller than the bandgap expected for $MAPbCl_3$ (~3.1 eV).[53] If in first order approximation we assume that the bandgap of $MAPbI_{3-x}Cl_x$ is a linear function of x between the two pure $MAPbCl_3$ and $MAPbI_3$ perovskite phases, the bandgaps measured by PTIR for the as-prepared sample would suggest that $\sim 0.06 < x^{local} < \sim 0.3$ (i.e., Cl/I < 10.0% mol/mol). This is a crude approximation but it provides an upper limit to the amount of Cl^- incorporated in the film. Because of the small x^{local} values analyzed in this work, such approximation appear reasonably justified by comparison with the bandgap dependence in $MAPb(I_{1-x}Br_x)_3$ that deviates from linearity only very weakly as a function of x across the whole composition range. Notably, the bandgap is progressively reduced at all locations as a function of annealing and after 30 min (sample A30) it reaches a value that is close to the bandgap of the $MAPbI_3$ reference sample at all locations: $0.00 < x^{local} < 0.06$ (i.e., Cl/I < 2.0% mol/mol). The PTIR spectra and the estimated local bandgap are helpful for interpreting the PTIR ratio maps in Figure 3. The red and blue colors in the ratio map at 702 nm denote Cl-poor regions and Cl-rich regions, respectively. The PTIR ratio maps (see bright red regions in Figure 3b,f,j,n) and the PTIR spectra (Figure 4) suggest that the chloride content in the film is progressively reduced with

DOI: 10.1021/acs.nanolett.5b03556
Nano Lett. 2015, 15, 8114–8121

annealing because the bandgap becomes smaller in all locations, most likely due to the sublimation of MACl, as previously suggested.[14,15,19,20]

Another beneficial effect of chloride is the improved stability of $MAPbI_{3-x}Cl_x$ films with respect to the $MAPbI_3$ phase.[17] Recently PTIR was used to study in situ the surface decomposition of $MAPbI_3$ films for annealing at 140 °C.[40] For $MAPbI_3$, changes in the surface topography and PTIR images occur within 10 min of annealing, which are followed by a large increase in the surface roughness for prolonged heating, resulting from the reduction of MA^+ content in the film (Supporting Information Figure S6). In contrast, the topography and PTIR absorption images of the $MAPbI_{3-x}Cl_x$ film (Figure 5) show much smaller changes for annealing at 140 °C

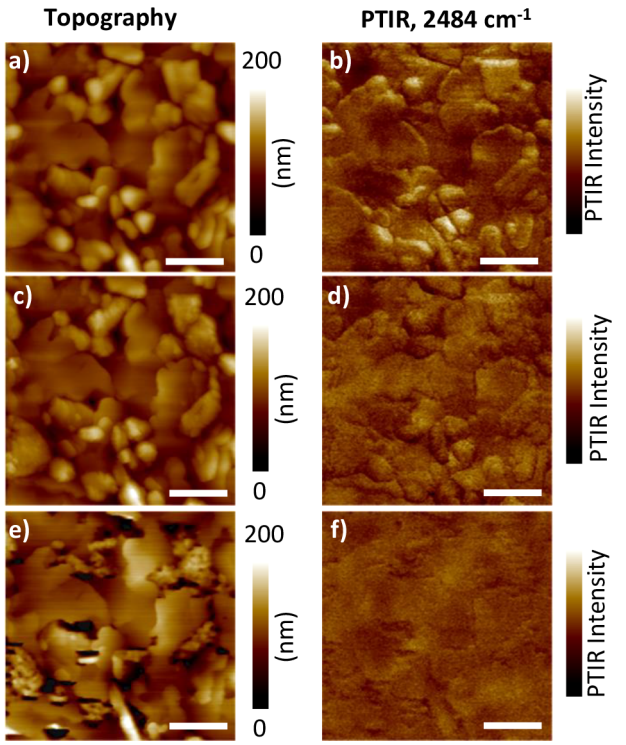

Figure 5. Stability of the $MAPbI_{3-x}Cl_x$ perovskite: Pairs of AFM topography and PTIR vibrational absorption images at 2484 cm^{-1} (corresponding to a combination of NH_3 symmetric bending CH_3 rocking)[44] for the $MAPbI_{3-x}Cl_x$ sample before annealing (a,b), after annealing at 140 °C for 10 min (c,d) and after annealing at 140 °C for additional 50 min (e,f). The intensity of the PTIR maps are plotted with the same scale range and all scale bars are 1.0 μm.

up to 60 min. In particular, some small grains appear to degrade but several larger grains appear to be stable for the whole duration of the experiments resulting in a smooth film.

In summary, $MAPbI_3$ and $MAPbI3_{-x}Cl_x$ perovskite films were prepared with a multicycle coating process and characterized with the PTIR technique to assess the local bandgap in annealed films, a measurement that provides evidence for the presence and spatial distribution at the nanoscale of chloride ions. Results show that after a mild annealing process (60 °C, 60 min), Cl^- ions are heterogeneously distributed in the $MAPbI_{3-x}Cl_x$ film. The local Cl^- content was estimated from the local bandgap to be as high as ~10% (x = 0.3). Upon further annealing, the local bandgap in $MAPbI_{3-x}Cl_x$ approaches the typical bandgap of $MAPbI_3$, suggesting that the Cl^- content is progressively reduced and become less heterogeneous (Cl^- between 0% and 2%). It is deduced that the mixed halide perovskite film initially consists of a mixture of Cl-rich and Cl-poor phases that upon annealing evolve into a homogeneous Cl-poorer phase by expelling MACl. Additionally, although the Cl^- content after annealing is small, the $MAPbI_{3-x}Cl_x$ sample shows much better thermal stability than the prototypical $MAPbI_3$ material.

EXPERIMENTAL SECTION

Fabrication of Perovskite Films. Perovskite samples for PTIR analysis were fabricated directly on a zinc sulfide right angle prism coated by a thin layer of PEDOT:PSS at a frequency of 50 Hz using a custom spinner adaptor. Perovskite films were fabricated using multicycle coating method as described by Dong et al.[12] In the first coating cycle, a hot (80 °C) PbI_2 solution (50% g/g mass fraction, DMF) was spun (50 Hz) onto the PEDOT:PSS coated substrate. Then, 10 μL of a MAI or of MAI/MACl (4:1 mol/mol) solution (2.4% g/g mass fraction) was dripped onto the PbI_2 film every 3 s during continuous spinning of substrate (50 Hz). After six MAI (or MAI/MACl), coating-cycles, the film was transferred onto a preheated hot plate for drying/annealing.

XRD Characterization. XRD measurements were performed with an X-ray diffractometer with Bragg–Brentano parafocusing geometry, a diffracted beam monochromator, and a conventional copper target X-ray tube operated at 40 kV and 30 mA.

Solar Cell Characterization. The photocurrent curves were measured in a N_2 filled glovebox under simulated 100 $mW{\cdot}cm^{-2}$ (AM 1.5 G) irradiation using a Xenon-lamp-based solar simulator. A visible-color glass-filtered Si diode was used to calibrate the light intensity before photocurrent measurement to avoid optical mismatch. The device area was 9 mm^2. The illuminated area was ~9 cm^2 with uniform light intensity.

PTIR Characterization. PTIR experiments were carried out using a modified commercial PTIR setup that consists of an AFM microscope operating in contact mode and three tunable pulsed laser sources (laser A, B, C) that have been described previously.[26,42] Two of the three laser sources (Laser A and Laser C) were used in this work. Laser A consists of a Q-switched diode pumped Nd:YAG laser (1064 nm), one optical parametric oscillator (OPO) based on a periodically poled lithium niobate (PPLN) crystal and a second OPO based on a noncritically phase-matched ZnGeP2 (ZGP) crystal. Laser A emits 10 ns pulses that are tunable from 4000 to ~1025 cm^{-1} (from 2.5 to 9.76 μm) at 1 kHz repetition rate and with line widths between 5 and 16 cm^{-1} depending on the wavelength. Laser C consists of a nanosecond Q-switched diode pumped Nd:YAG pump laser and an OPO based on a beta barium borate nonlinear crystal integrated into a single enclosure. Laser C emits 10 ns pulses with <1 nm line width at 1 kHz repetition rate in the range from 400 to 2300 nm. The low repetition rate of the laser assures that a new pulse will excite a sample and cantilever after they have returned to equilibrium. The typical laser spot size is ~30 μm at the sample.

PTIR spectra were obtained by averaging the cantilever deflection amplitude from 256 individual laser pulses at each wavelength and tuning the laser at intervals of 4 and 50 cm^{-1} for laser A and C, respectively. PTIR images were recorded by illuminating the sample with a constant wavelength while scanning the AFM tip. The AFM height and the PTIR signal acquisition was synchronized so that for each AFM pixel the

DOI: 10.1021/acs.nanolett.5b03556
Nano Lett. 2015, 15, 8114–8121

PTIR signal is an average over 32 laser pulses. The pixel sizes are 50 nm × 50 nm in all images. The pixel-by-pixel PTIR absorption image ratios were obtained by cross correlating the simultaneously recorded topography images to compensate for any eventual image drift. Commercially available 450 μm long silicon contact-mode AFM probes with a nominal spring constant between 0.07 N/m and 0.4 N/m were used.

To ensure that the observed bandgap changes were induced by the sample annealing process and not by laser heating consecutive sets of PTIR measurements were obtained (the second set as a control) before annealing and after each annealing step to ensure that changes occurred only between annealing steps and not between consecutive PTIR measurements.

FTIR Characterization. Fourier transfer infrared (FTIR) spectra were recorded using a diamond attenuated reflection accessory. One hundred and twenty-eight spectra (4 cm^{-1} resolution) were acquired and averaged for each sample.

■ ASSOCIATED CONTENT

Supporting Information

The Supporting Information is available free of charge on the ACS Publications website at DOI: 10.1021/acs.nanolett.5b03556.

Summary of annealing cycles, FTIR and PTIR spectra of MACl and MAI compounds, and additional PTIR maps and spectra. (PDF)

■ AUTHOR INFORMATION

Corresponding Authors

*E-mail: (A.C.) andrea.centrone@nist.gov.
*E-mail: (J.H.) jhuang2@unl.edu.

Author Contributions

The manuscript was written through contributions of all authors. All authors have given approval to the final version of the manuscript.

Funding

We thank the partial financial support from National Science Foundation Grant awards DMR-1505535 and 1538893.

Notes

The authors declare no competing financial interest.

■ ACKNOWLEDGMENTS

J.C. and B.L. acknowledges support under the Cooperative Research Agreement between the University of Maryland and the National Institute of Standards and Technology Center for Nanoscale Science and Technology, Award 70NANB10H193, through the University of Maryland.

■ ABBREVIATIONS

PTIR, photothermal induced resonance; XPS, X-ray photoelectron spectroscopy; STEM-EDS, scanning transmission electron microscopy with energy dispersive spectroscopy; XRD, X-ray diffraction; AFM, atomic force microscopy

■ REFERENCES

(1) Zhou, H.; Chen, Q.; Li, G.; Luo, S.; Song, T.-b.; Duan, H.-S.; Hong, Z.; You, J.; Liu, Y.; Yang, Y. *Science* **2014**, *345*, 542−546.
(2) Xiao, Z.; Bi, C.; Shao, Y.; Dong, Q.; Wang, Q.; Yuan, Y.; Wang, C.; Gao, Y.; Huang, J. *Energy Environ. Sci.* **2014**, *7*, 2619−2623.
(3) Xiao, Z.; Dong, Q.; Bi, C.; Shao, Y.; Yuan, Y.; Huang, J. *Adv. Mater.* **2014**, *26*, 6503−6509.
(4) Bi, C.; Dong, Q.; Shao, Y.; Wang, Q.; Yuan, Y.; Xiao, Z.; Huang, J.; Nat. *Nat. Commun.* **2015**, *6*, 7747.
(5) Jeon, N. J.; Noh, J. H.; Yang, W. S.; Kim, Y. C.; Ryu, S.; Seo, J.; Seok, S. I. *Nature* **2015**, *517*, 476−480.
(6) Stranks, S. D.; Eperon, G. E.; Grancini, G.; Menelaou, C.; Alcocer, M. J.; Leijtens, T.; Herz, L. M.; Petrozza, A.; Snaith, H. J. *Science* **2013**, *342*, 341−344.
(7) Xing, G.; Mathews, N.; Sun, S.; Lim, S. S.; Lam, Y. M.; Grätzel, M.; Mhaisalkar, S.; Sum, T. C. *Science* **2013**, *342*, 344−347.
(8) Dong, Q.; Fang, Y.; Shao, Y.; Mulligan, P.; Qiu, J.; Cao, L.; Huang, J. *Science* **2015**, *347*, 967−970.
(9) Shi, D.; Adinolfi, V.; Comin, R.; Yuan, M.; Alarousu, E.; Buin, A.; Chen, Y.; Hoogland, S.; Rothenberger, A.; Katsiev, K. *Science* **2015**, *347*, 519−522.
(10) Liu, M.; Johnston, M. B.; Snaith, H. J. *Nature* **2013**, *501*, 395−398.
(11) Chen, Q.; Zhou, H.; Fang, Y.; Stieg, A. Z.; Song, T.-B.; Wang, H.-H.; Xu, X.; Liu, Y.; Lu, S.; You, J.; Sun, P.; McKay, J.; Goorsky, M. S.; Yang, Y. *Nat. Commun.* **2015**, *6*, 7269.
(12) Dong, Q.; Yuan, Y.; Shao, Y.; Fang, Y.; Wang, Q.; Huang, J. *Energy Environ. Sci.* **2015**, *8*, 2464−2470.
(13) Dar, M. I.; Arora, N.; Gao, P.; Ahmad, S.; Grätzel, M.; Nazeeruddin, M. K. *Nano Lett.* **2014**, *14*, 6991−6996.
(14) Yu, H.; Wang, F.; Xie, F.; Li, W.; Chen, J.; Zhao, N. *Adv. Funct. Mater.* **2014**, *24*, 7102−7108.
(15) Unger, E. L.; Bowring, A. R.; Tassone, C. J.; Pool, V. L.; Gold-Parker, A.; Cheacharoen, R.; Stone, K. H.; Hoke, E. T.; Toney, M. F.; McGehee, M. D. *Chem. Mater.* **2014**, *26*, 7158−7165.
(16) Colella, S.; Mosconi, E.; Pellegrino, G.; Alberti, A.; Guerra, V. L.; Masi, S.; Listorti, A.; Rizzo, A.; Condorelli, G. G.; De Angelis, F.; Gigli, G. *J. Phys. Chem. Lett.* **2014**, *5*, 3532−3538.
(17) Chen, Y.; Chen, T.; Dai, L. *Adv. Mater.* **2015**, *27*, 1053−1059.
(18) Xie, F. X.; Zhang, D.; Su, H.; Ren, X.; Wong, K. S.; Grätzel, M.; Choy, W. C. H. *ACS Nano* **2015**, *9*, 639−646.
(19) Colella, S.; Mosconi, E.; Fedeli, P.; Listorti, A.; Gazza, F.; Orlandi, F.; Ferro, P.; Besagni, T.; Rizzo, A.; Calestani, G. *Chem. Mater.* **2013**, *25*, 4613−4618.
(20) Williams, S. T.; Zuo, F.; Chueh, C.-C.; Liao, C.-Y.; Liang, P.-W.; Jen, A. K.-Y. *ACS Nano* **2014**, *8*, 10640−10654.
(21) Zhao, Y.; Zhu, K. *J. Phys. Chem. C* **2014**, *118*, 9412−9418.
(22) Xing, G.; Mathews, N.; Lim, S. S.; Yantara, N.; Liu, X.; Sabba, D.; Grätzel, M.; Mhaisalkar, S.; Sum, T. C. *Nat. Mater.* **2014**, *13*, 476−480.
(23) Tan, Z.-K.; Moghaddam, R. S.; Lai, M. L.; Docampo, P.; Higler, R.; Deschler, F.; Price, M.; Sadhanala, A.; Pazos, L. M.; Credgington, D. *Nat. Nanotechnol.* **2014**, *9*, 687−692.
(24) Dazzi, A.; Prazeres, R.; Glotin, E.; Ortega, J. M. *Opt. Lett.* **2005**, *30*, 2388−2390.
(25) Lahiri, B.; Holland, G.; Centrone, A. *Small* **2013**, *9*, 439−445.
(26) Katzenmeyer, A. M.; Aksyuk, V.; Centrone, A. *Anal. Chem.* **2013**, *85*, 1972−1979.
(27) Felts, J. R.; Kjoller, K.; Lo, M.; Prater, C. B.; King, W. P. *ACS Nano* **2012**, *6*, 8015−8021.
(28) Centrone, A. *Annu. Rev. Anal. Chem.* **2015**, *8*, 101−126.
(29) Van Eerdenbrugh, B.; Lo, M.; Kjoller, K.; Marcott, C.; Taylor, L. S. *Mol. Pharmaceutics* **2012**, *9*, 1459−1469.
(30) Katzenmeyer, A. M.; Canivet, J.; Holland, G.; Farrusseng, D.; Centrone, A. *Angew. Chem., Int. Ed.* **2014**, *53*, 2852−2856.
(31) Dazzi, A.; Prazeres, R.; Glotin, F.; Ortega, J. M.; Al-Sawaftah, M.; de Frutos, M. *Ultramicroscopy* **2008**, *108*, 635−641.
(32) Marcott, C.; Lo, M.; Kjoller, K.; Prater, C.; Noda, I. *Appl. Spectrosc.* **2011**, *65*, 1145−1150.
(33) Ramer, G.; Balbekova, A.; Schwaighofer, A.; Lendl, B. *Anal. Chem.* **2015**, *87*, 4415−4420.
(34) Ruggeri, F. S.; Longo, G.; Faggiano, S.; Lipiec, E.; Pastore, A.; Dietler, G. *Nat. Commun.* **2015**, *6*, 7831.
(35) Lahiri, B.; Holland, G.; Aksyuk, V.; Centrone, A. *Nano Lett.* **2013**, *13*, 3218−3224.

DOI: 10.1021/acs.nanolett.5b03556
Nano Lett. 2015, 15, 8114−8121

(36) Katzenmeyer, A. M.; Chae, J.; Kasica, R.; Holland, G.; Lahiri, B.; Centrone, A. *Adv. Opt. Mater.* **2014**, *2*, 718−722.
(37) Aksyuk, V.; Lahiri, B.; Holland, G.; Centrone, A. *Nanoscale* **2015**, *7*, 3634−3644.
(38) Ghosh, S.; Kouamé, N. A.; Ramos, L.; Remita, S.; Dazzi, A.; Deniset-Besseau, A.; Beaunier, P.; Goubard, F.; Aubert, P.-H.; Remita, H. *Nat. Mater.* **2015**, *14*, 505−511.
(39) Morsch, S.; Lyon, S.; Greensmith, P.; Smith, S. D.; Gibbon, S. R. *Faraday Discuss.* **2015**, *180*, 527−542.
(40) Dong, R.; Fang, Y.; Chae, J.; Dai, J.; Xiao, Z.; Dong, Q.; Yuan, Y.; Centrone, A.; Zeng, X. C.; Huang, J. *Adv. Mater.* **2015**, *27*, 1912−1918.
(41) Yuan, Y.; Chae, J.; Shao, Y.; Wang, Q.; Xiao, Z.; Centrone, A.; Huang, J. *Adv. Energy Mater.* **2015**, *5*, 1500615.
(42) Katzenmeyer, A. M.; Holland, G.; Kjoller, K.; Centrone, A. *Anal. Chem.* **2015**, *87*, 3154−3159.
(43) Dazzi, A.; Glotin, F.; Carminati, R. *J. Appl. Phys.* **2010**, *107*, 124519.
(44) Cabana, A.; Sandorfy, C. *Spectrochim. Acta* **1962**, *18*, 843−861.
(45) Frost, J. M.; Butler, K. T.; Brivio, F.; Hendon, C. H.; van Schilfgaarde, M.; Walsh, A. *Nano Lett.* **2014**, *14*, 2584−2590.
(46) Mosconi, E.; Quarti, C.; Ivanovska, T.; Ruani, G.; De Angelis, F. *Phys. Chem. Chem. Phys.* **2014**, *16*, 16137−16144.
(47) Poglitsch, A.; Weber, D. *J. Chem. Phys.* **1987**, *87*, 6373−6378.
(48) Quarti, C.; Grancini, G.; Mosconi, E.; Bruno, P.; Ball, J. M.; Lee, M. M.; Snaith, H. J.; Petrozza, A.; Angelis, F. D. *J. Phys. Chem. Lett.* **2014**, *5*, 279−84.
(49) Brivio, F.; Walker, A. B.; Walsh, A. *APL Mater.* **2013**, *1*, 042111.
(50) Wang, Y.; Gould, T.; Dobson, J. F.; Zhang, H.; Yang, H.; Yao, X.; Zhao, H. *Phys. Chem. Chem. Phys.* **2014**, *16*, 1424−1429.
(51) Frost, J. M.; Butler, K. T.; Walsh, A. *APL Mater.* **2014**, *2*, 081506.
(52) Noh, J. H.; Im, S. H.; Heo, J. H.; Mandal, T. N.; Seok, S. I. *Nano Lett.* **2013**, *13*, 1764−1769.
(53) Hu, M.; Bi, C.; Yuan, Y.; Xiao, Z.; Dong, Q.; Shao, Y.; Huang, J. *Small* **2015**, *11*, 2164−2169.

DOI: 10.1021/acs.nanolett.5b03556
Nano Lett. 2015, 15, 8114−8121